

Effects of morphology on phonons of nanoscopic silver grains

Gustavo A. Narvaez,^{1,*} Jeongnim Kim,^{2,3} and John W. Wilkins¹

¹*Department of Physics, The Ohio State University, Columbus, Ohio 43210*

²*Materials Computation Center, University of Illinois, Urbana-Champaign, Illinois 61801*

³*National Center for Supercomputer Applications,
University of Illinois, Urbana-Champaign, Illinois 61801*

(Dated: December 2, 2024)

The morphology of nanoscopic Ag grains significantly affects the phonons. Atomistic simulations show that realistic nanograin models display complex vibrational properties. (1) Single-crystalline grains. Nearly-pure torsional and radial phonons appear at low frequencies. For low-energy, faceted models, the breathing mode and acoustic gap (lowest frequency) are about 10% lower than predicted by elasticity theory (ET) for a continuum sphere of the same volume. The sharp edges and the atomic lattice split the ET-acoustic-gap quintet into a doublet and triplet. The surface protrusions associated with nearly spherical, high-energy models produce a smaller acoustic gap and a higher vibrational density of states (DOS) at frequencies $\nu < 2$ THz. (2) Twined icosahedra. In contrast to the single-crystal case, the inherent strain produce a larger acoustic gap, while the core atoms yield a DOS tail extending beyond the highest frequency of single-crystalline grains. (3) Mark's decahedra, in contrast to (1) and (2), do not have a breathing mode; although twined and strained, do not exhibit a high-frequency tail in the DOS. (4) In irregular nanograins, grain boundaries and surface disorder yield non-degenerate phonon frequencies, and significantly smaller acoustic gap. Only these nanograins exhibit a low-frequency ν^2 DOS in the interval 1-2THz.

I. INTRODUCTION

Recent experiments have probed the size dependence of the electronic-energy relaxation rate in nanoscopic metal grains.^{1,2,3} Perhaps the most striking aspect of these experiments is the finding of Arbouet and coworkers which shows that the electron-phonon relaxation rate τ_{ep} does not depend on the environment of the grains.¹ Gold and silver grains suspended in solution present the same size dependence of τ_{ep} than those embedded in a solid matrix (e.g., Al_2O_3).

To explain the data, current models for the energy relaxation of hot electrons due to electron-phonon coupling in nanoscopic grains rely on phenomenological parameters and simplifications. (For example, replacing the vibrational density of states with the Debye model.) One has to keep in mind, however, that the experiments involved several materials (Ag, Au, Pt) with a wide range of grain sizes, where a myriad of stable low-energy morphologies has been observed and proposed.^{4,5,6,7} Thus, to understand the electron-phonon coupling in nanoscopic metal grains it would be desirable to have a description of their vibrational properties that includes the grain's morphology: facets, grain boundaries, and surface disorder and defects.

There are papers in the literature that have addressed the vibrational density of states of nanoscopic metal grains using ideal, spherical models^{8,9,10} Unfortunately, the use of these idealized models limits a detailed understanding of the vibrational properties and the role of morphology. Furthermore, the idealized models neglect the influence of grain boundaries, and surface disorder and defects on the vibrational properties of the experimental nanograins.¹¹ In this work we focus on *realistic*, nanoscopic Ag grains containing 150-1400 atoms

and atomistically simulate their vibrational properties, by calculating the phonon frequencies and displacement vectors. We show that morphology introduces a high degree of complexity in the phonon spectra; total and partial vibrational density of states; and phonon localization.

Our predictions, which should be general for nanoscopic metals, show the following prominent features. (a) Low-energy, single-crystalline grains present nearly-pure torsional and radial phonon modes. The frequencies of the breathing mode and the acoustic gap (lowest frequency) are nearly 10% lower than predicted by elasticity theory (ET) for a continuum sphere.^{12,13,14} The sharp edges and atomic lattice of the grains lead to the splitting of the acoustic gap quintet predicted by ET in a doublet and triplet, where the magnitude of the splitting depends on the relative number of atoms at the boundary of different facets. High-energy, ideal spherical models present regular protrusions on the surface. When compared to a faceted grain of the same size, these protrusions lead to a smaller acoustic gap, which is not necessarily degenerate; and to a higher total vibrational density of states (DOS) at frequencies $\nu < 2$ THz.

(b) As in the case of single-crystalline nanograins, twined icosahedra have a breathing mode. Strain in these grains leads to a higher acoustic gap, and a high-frequency tail in the DOS that extends beyond the highest frequency in single-crystalline grains. On the other hand, twined and strained Mark's decahedra *do not* have a breathing mode, neither exhibit a high-frequency tail on DOS.

(c) Irregular nanograins with grain boundaries and surface disorder do not have degenerate phonon frequencies, and the acoustic gap is significantly reduced. These nanograins are the only ones to exhibit ν^2 DOS in the

interval 1-2THz. The extent of this region depends on the nature of disorder.

To summarize, our simulations show the complexity of the vibrational properties of nanoscopic metals, and point out similarities between the vibrational density of states of nanograins with grain boundaries and surface disorder and that of massive nanocrystalline samples. This work is a required step towards understanding the size dependence of the electron-phonon coupling in nanoscopic metal grains.

II. NANOGRAINS' MORPHOLOGY AND ENERGETICS

The morphology of a nanograin is specified by the number of atoms N , shape and atomic arrangement. The shape refers to the symmetry and facets, while the atomic arrangement pertains to the nanograin's crystalline characteristics: single-crystalline, twined, surface-disordered and defective. Here, we classify the model nanograins—with sizes that range from $N=150$ -1400—in three broad classes:

(I) Single-crystalline nanograins derived from the face-centered-cubic lattice of Ag with facets oriented in the $[111]$, $[001]$, and $[101]$ directions (depending on size). Figure 1(a) illustrates class I grains. TO and TO^+ originate from different degrees of truncation of an octahedron (Oh). TO's are regular in the sense that the number of atoms in every edge is the same and the $[111]$ and $[001]$ facets form regular hexagons and squares, respectively. TO^+ represents a group of grains that result from removing the vertices of the Oh first and then $[001]$ facets until reaching the TO. The latter protocol leads to grains that have more atoms in the edges connecting $[111]$ facets than in the $[111]/[001]$ boundary. Model C results from truncating cuboctahedra. In these grains, $[001]$ facets are larger than the corresponding facets in TO^+ , while the geometry of $[111]$ facets is preserved. On the other hand, by simply removing the atoms lying in the $[111]$ -facets boundary, Model C leads to Model H. By construction, Model H nanograins show $[101]$ facets.

(II) Twined icosahedra (lh) and its variants,¹⁵ and Mark's decahedra (M-Dh). Examples of lh and M-Dh appear in Fig. 1. Both these grains are described in detail in the literature.^{16,17} lh's are strained and feature $[111]$ facets, 12 vertices, 20 internal grains, and six 5-fold axis; one of them appears indicated with a "5" in Fig. 1. In contrast, M-Dh's are less strained, have multiple faceting and a single 5-fold axis.

(III) Complex, partially disordered multigrain nanograins that have grain boundaries, surface disorder, and defects; see Fig. 1(c). Simulated annealing is used to generate these grains. The most common surface defects are vertex vacancies [shown in grey in Fig. 1(c)], terraces, and stacking faults. In most cases, the grain boundaries lead to 5-fold-like axis and a high number (about 10) of internal grains. However, we have also

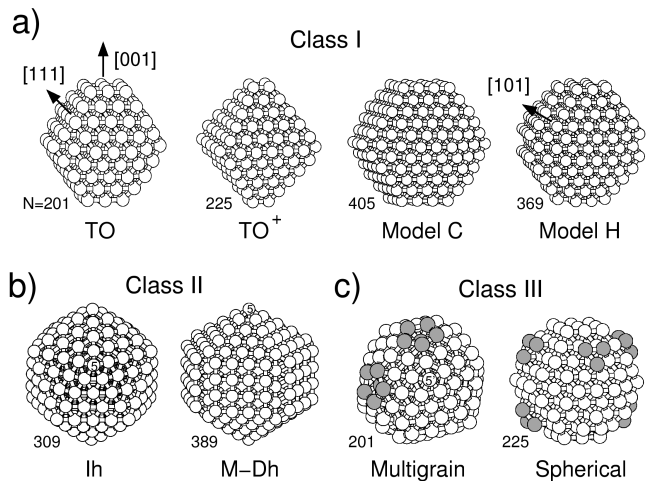


FIG. 1: Classes of Ag nanograins illustrated with selected specimens. "5" [(b)] and "5'" [(c)] indicate, respectively, a 5-fold and 5-fold-like axis. Number of atoms (N) is indicated. (a) Single-crystal grains with $[111]$ and $[001]$ facets in the regular (TO) and irregular (TO^+) truncated octahedron geometry. Compared to TO^+ , Model C has bigger $[001]$ facets and similar $[111]$ -facet geometry. Model H grains present $[110]$ facets. (b) Twined icosahedron (lh) and Mark's decahedron (M-Dh). (c) Multigrain nanograins exhibit grain boundaries and surface disorder; gray atoms highlight vertex vacancies. Spherical nanograins result from decorating regular, faceted specimens. Gray atoms decorating $[111]$ facets of TO [see (a)] yield the shown "sphere."

encountered multigrains with a single twin boundary or internal stacking fault.

We also include in class III the so-called *spherical* nanograins [Figure 1(c)]. Despite their unrealistic morphology, these grains have been the model of choice in recent simulations of the vibrational properties of nanoscopic metal grains.^{8,10} Although single-crystalline, these grains have small protrusions (grey atoms in the figure) on the $[111]$ and, depending on size, $[001]$ facets of otherwise compact specimens. These protrusions act as surface defects, despite of being highly regular. (Indeed, one may consider the compact nanograins to be *decorated* by the protrusions. These surface defects contribute to the higher energies of the spherical nanograins relative to other structures and are removed by simulated annealing starting at high temperatures.

Figure 2 shows the effect of morphology on the total energy \mathcal{E} for class I and II. lh are the most stable grains up to $N \simeq 600$, where the cohesive energies of lh, M-Dh and TO are effectively degenerate. For larger grains, strain dominates over efficient faceting and single-crystalline grains become more stable. TO^+ splits into two *bands*, indexed by the number of atoms in $[111]$ -facet boundaries; the lower and upper bands corresponding to 5 and 7 atoms, respectively. The lower and upper band merge at $N = 1289$ and $N = 1975$, respectively, with TO energies. Model H tracks the TO^+ upper band. Mark's decahedra show significant fluctuations in the size depen-

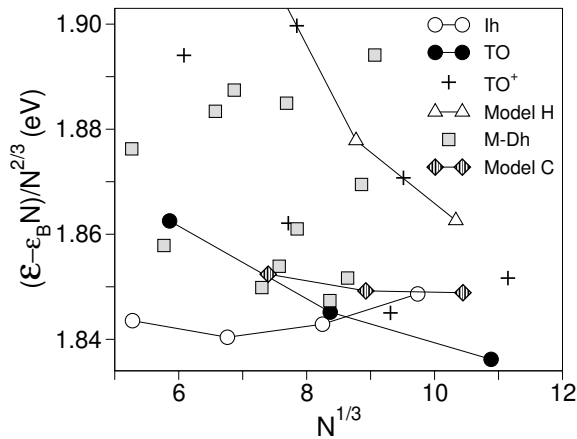


FIG. 2: Morphology effects on the total energy \mathcal{E} of grains in Fig. 1(a) and (b). \mathcal{E} is measured relative to bulk ($\varepsilon_B = 2.85$ eV). Twined icosahedra (Ih) are the most stable structures from 150 to $N \simeq 600$; where the cohesive energies of Ih, M-Dh, and TO are nearly degenerate. The energy of TO^+ nanograins separates in two *bands* (see Sec. II). The upper band follows the progression of Model H. Increased faceting is responsible for the noticeable scattering in M-Dh's energy.

dence of \mathcal{E} due to increased faceting; which permits generating M-Dh grains with significantly different *sphericity* even if the number of atoms is slightly changed.¹⁸

Considering the energetics of class III, Table I lists the total energies of multigrain and spherical nanograins. These energies exceed by a considerable amount those of class I and II. Nonetheless, multigrain nanograins are non-equilibrium structures that are likely to exist under experimental conditions. In addition, the recent simulations of the structure of ultra-small Al clusters (Maninen *et al.*, in Ref. 18) show that complex, multigrain structures are competitive with those of class I and II. Spherical grains, on the other hand, correspond to an idealization of realistic metal grains and are presented here only for comparison purposes.

TABLE I: Total energy of multigrain and spherical Ag grains vs number of atoms N . Here, $\varepsilon_B = 2.85$ eV is the bulk cohesive energy.

	$(\mathcal{E} - \varepsilon_B N)/N^{2/3}$ (eV)			
N	225	459	783	1289
Multigrain	1.93	1.94	1.98	
Spherical	2.06	2.06	1.99	2.04

III. VIBRATIONAL PROPERTIES

We show that nanograin morphology strongly affects the vibrational properties. By using the methods described in the Appendix, we analyze the effect of nanograin's morphology on the phonon frequency spec-

trum, vibrational density of states (DOS), and phonon localization. First, we describe general features of phonon spectra followed by a comparison between class I and spherical grains with class II and multigrains. Second, we contrast the DOS of TO with class II and III nanograins. Finally, we focus on $N=459$ nanograins in class I and III to illustrate important features of the phonon localization.

A. Phonon frequencies

General features. The finite size of the grains lead to discrete phonon spectra. The acoustic gap, which is defined as the value of the lowest phonon frequency, decreases with size due to confinement. Our simulations show that the acoustic gap roughly scales as $N^{-1/3}$, as predicted by elasticity theory (ET) for a finite grain,¹² and its magnitude depends on morphology. Each grain in class I as well as icosahedra (Ih) have a nearly-radial, breathing mode. In contrast, this mode does not appear in Mark's decahedra (M-Dh) or multigrains (class III). When compared with predictions of elasticity theory for a solid sphere with the same volume as the nanograins, our simulations lead to frequencies of the breathing mode (R_1) and acoustic gap about 10% smaller. For R_1 , ET predicts $\nu_\rho^N = 2.825 (c_l/2\pi R)$, where R is the radius of the sphere and $c_l = 3686$ m/s is the average longitudinal sound velocity of bulk silver.¹⁹ The ET-acoustic-gap equals $0.401 \nu_\rho^N$ with 5-fold degeneracy.^{13,14}

Class I and spherical nanograins. For TO, TO^+ , and Model C in class I, and for the spherical grains in class III, Figure 3 shows phonon frequencies up to the first nearly-radial, breathing mode. Main features are the following. (i) All grains show frequencies that are either non-degenerate or 2-fold and 3-fold degenerate. (ii) The five lowest frequencies split into a triplet and a doublet; a gap separates this cluster from other frequencies. This triplet-doublet cluster originates from symmetry breaking of the ET-acoustic-gap quintet. The size dependence of the small split-off separation between the triplet and doublet depends on the morphology. It decreases for TO, and in TO^+ , $N=459$ the triplet and doublet even switch order. Model C shows a more remarkable size dependence: The split-off separation remains nearly constant and similar to that of $N=201$ TO grain. We attribute this behavior to the fixed number of atoms (3) in the [111]-facet boundaries. (iii) In TO^+ and in 586 and 1289 TO grains, a distinguishable, second group of frequencies appears; a triplet precedes a doublet and two triplets follow. The separation between multiplets in these complexes also depend upon the size of the nanograin. In contrast, no visible gap separates these frequencies in Model C and 201, TO. At frequencies higher than $0.5\nu_\rho^N$ no sizeable gaps appear in any grain. (iv) In all grains, near to the lowest triplet-doublet, we find a low-frequency nearly-torsional edge mode T_1 ; morphology dramatically affects the size dependence of its frequency (Fig. 3). In TO,

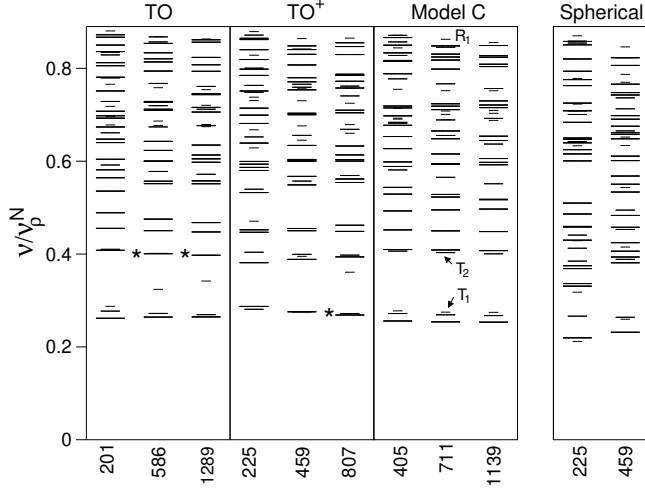


FIG. 3: Single-crystalline Ag grains' scaled phonon frequencies ν up to the first nearly-radial, breathing mode (R_1). $\nu_p^N = 2.825(c_l/2\pi R)$ (see Sec. III A). Frequencies are either nondegenerate (short dash) or 2-fold (medium dash) and 3-fold (long dash) degenerate frequencies are present. In TO, TO^+ and Model C, the low-lying phonon frequency structure is qualitatively similar except for T_1 ; a nearly-torsional, edge vibration (see Fig. 4). T_2 labels a 2-fold degenerate twist mode. Asterisks (*) indicate nearly degenerate doublet-triplet clusters. Surface protrusions yield different low-frequency phonon structure in spherical grains.

T_1 's frequency remains almost constant while in TO^+ it decreases with the surface. In Model C, it scales as ν_p^N and is *locked* with the lowest five frequencies.

The ideal spherical nanograins present phonon frequencies that are nondegenerate as well 2- and 3-fold degenerate. Contrary to class I grains, the low-lying frequencies present a less clear pattern. These grains, $N=225$ and 459 , may be viewed as the *decorated* version of the 201 TO (c.f. Fig. 1) and 405 TO^+ , respectively. The coupling between the vibration of the protrusions and the atoms in the faceted grain that they decorate reduces the acoustic gap. This coupling also destroys the similarities between the frequency structure in 201 and 405. (See Fig. 2.)

For $N=586$ TO nanograin, Fig. 4(a) shows representations of the displacement vectors of 3 selected phonon modes. As mentioned above, T_1 is nearly torsional and the atoms surrounding the edges have the higher amplitude. T_2 is one of the two nearly-torsional, 2-fold degenerate twist modes. In contrast to T_1 , T_2 's frequency depends less strongly on morphology (see Fig. 3). T_1 and T_2 also appear in spherical grains. R_1 is the non-degenerate, nearly-radial breathing mode. It should be noted that TO and lh grains have another nearly-torsional mode T_3 (not shown), which is an excited, non-degenerate twist mode. This mode does not appear in any other single-crystalline grain or Mark decahedron, as only TO's and lh's have the same number of atoms at the every [111]-facet boundary. [c.f. Figure 1(a) and (b)]

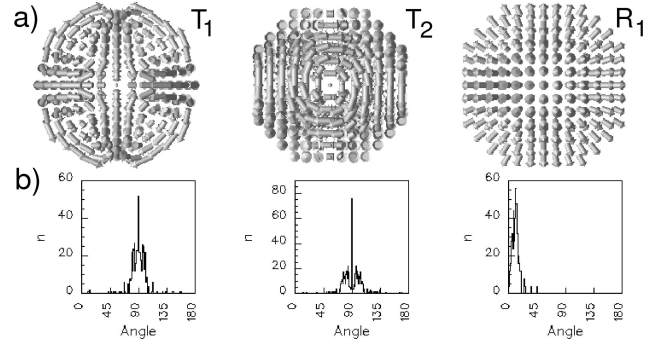


FIG. 4: (a) Displacement vectors of selected phonon modes in the $N=586$, TO nanograin: (i) T_1 , a non-degenerate mode in which the atoms surrounding the edges have a significant amplitude, (ii) T_2 , one of the doubly-degenerate twist modes, and (iii) R_1 , the first nearly-radial, breathing mode. (b) Distribution functions (1° bin size) of the angle between the equilibrium vector position of an atom—measured from the center of the grain—and its displacement vector. The distributions peak around 90° for T_1 and T_2 , and 10° (instead zero) for R_1 , respectively. For larger grains the distributions peak around $2-4^\circ$.

For T_1, T_2, R_1 , figure 4(b) shows histograms of the angles between the displacement vector of atom i (\vec{u}^i) and its equilibrium position (\vec{R}^i); measured from the center of the grain. [The angle is defined $\text{mod}(\pi)$.] The purpose is to show the extent to which the crystalline field and edges of the grains couple angular and radial degree's of freedom. Note that in an ideal elastic sphere, torsional and breathing modes have angular- and radial-only displacements, respectively.¹³ The values for the average angle $\bar{\theta}$ and the standard deviation σ of the histograms in Fig. 4 are the following: $\bar{\theta}_{T_1} = 89.51^\circ$, $\sigma_{T_1} = 12.53^\circ$; $\bar{\theta}_{T_2} = 89.95^\circ$, $\sigma_{T_2} = 14.46^\circ$; and $\bar{\theta}_{R_1} = 10.64^\circ$, $\sigma_{R_1} = 5.96^\circ$. In general, as size increases, for nearly torsional and radial modes, $\bar{\theta}$ approaches 90° and 0° , respectively; and σ decreases.

Class II and multigrain nanograins. Figure 5(a) shows the phonon frequencies up to the first nearly-radial, breathing mode of twined icosahedra (lh). Panel (b) shows phonon frequencies up to ν_p^N for Mark's decahedra (M-Dh) and multigrain samples. (See Fig. 1.) Prominent features are the following:

(i) Strain in the icosahedra leads to clusters of non-degenerate frequencies. At higher frequencies a few 2-fold degeneracies appear. The acoustic gap is higher than in class I and spherical grains. It also has a triplet-doublet structure with higher split-off and no degeneracies. (ii) Mark's decahedra, like lh's, only show a few doubly degenerate frequencies over the entire spectrum. The acoustic gap is similar in magnitude to the gaps of class I and spherical grains. However, there is no resemblance of the triplet-doublet structure. More importantly, Mark's decahedra do not have breathing modes. The small [111]-oriented dents (see Fig. 1) may be responsible for these features. (iii) Multigrains only have

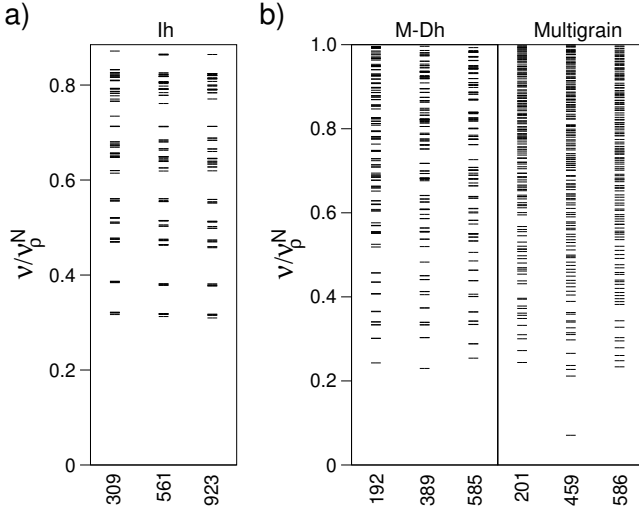


FIG. 5: (a) Equivalent to Fig. 3 but for twined icosahedral grains. Strain leads to clusters of non-degenerate frequencies, and acoustic gaps that are bigger than in single-crystalline grains and Mark's decahedra. (b) Mark's decahedra and multigrain's phonon frequencies up to ν_p^N . These two nanograins *do not have* nearly-radial phonon modes. Like lh's, M-Dh's show non-degenerate frequencies in this range. In multigrain, grain boundaries and surface disorder lead to non-degenerate frequencies and significantly smaller acoustic gap.

non-degenerate frequencies. Like M-Dh, multigrain do not have breathing modes. Surface disorder and defects reduce the acoustic gap. (Compare Fig. 3 and 4.) The lowest-lying modes are localized on the surface of the grain; however, the degree of localization is sample (disorder) dependent. In addition, the more localized the mode the softer its frequency. The visible gap between the lowest allowed phonon mode and the first *excited* vibration in the $N=459$ nanograin is disorder sensitive.

B. Vibrational density of states

Figure 6 shows the effects of morphology and size on the vibrational density of states (DOS) per atom $g(\nu)$. In these results, each $g(\nu)$ histogram has a 0.1 THz bin.²⁰ **TO grains.**—At low and high frequencies, $g(\nu)$ depends strongly on morphology. DOS in TO grains increase up to 2 THz, which correspond to a maximum in bulk DOS, originated by transversal phonons (TP). The longitudinal-phonon peaks around 4.7 THz have nearly the same amplitude for different sizes. Other class I grains (c.f. Sec. II) show a similar behavior. DOS extends to slightly higher frequencies for smaller grains. **Icosahedra and Mark's decahedra.**—In icosahedra, strain and twinning remarkably smear the LP peak in the DOS. Its intensity is lower than the TP peak about 2 THz, and remains roughly unchanged with increasing size. In addition, there is a frequency tail beyond the highest fre-

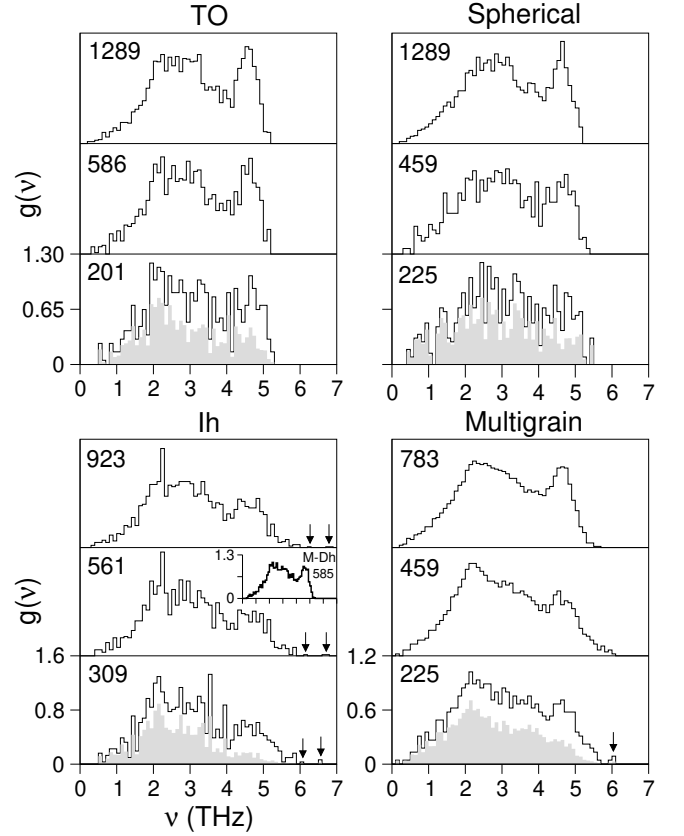


FIG. 6: Morphology and size effects on vibrational density of states $g(\nu)$. Shaded histograms show the partial density of states due to surface atoms. Bin size is 0.1 THz. At low and high frequencies, $g(\nu)$ depends significantly on geometrical details of the nanograins. Density of states at $\nu < 2$ THz is higher in spherical grains than in TO. For faceted and lh grains, the longitudinal-phonon (LP) peaks around 4.7 THz have nearly the same amplitude regardless of size. In contrast, LP's amplitude grows with grain size in multigrain and spherical grains. Grain boundaries in multigrain and twined lh lead to a frequency tail beyond the maximum value in single-crystalline grains. No tail is seen in Mark's decahedra, whereas the LP peak is visible. (See inset in panel lh, 561 for $g(\nu)$ of a 585 M-Dh.) Arrows indicate features arising from phonons strongly localized in the center of the grains.

quency in TO and spherical. Beyond 6 THz, the DOS show small features (arrows in Fig. 6, lh) that originate in a four phonon modes strongly localized at the center of the grains. These phonon modes consist of displacement of a few (5-40) atoms along the grain-boundary interfaces that meet at the center of grain. Removal of the center atom of the icosahedra results in the disappearance of these features in the density of states. Mark's decahedra show a DOS significantly different from icosahedra; see the inset in Fig. 6, panel lh, 561. Although M-Dh's are twined and strained, an LP peak is visible and its intensity remains nearly unchanged with size (not shown). More important, Mark's decahedra do not show a high-frequency tail in DOS. **Multigrain and spheri-**

cal nanograins.—In spherical grains, protrusions increase $g(\nu)$ below 2 and above 5 THz relative to faceted grains. Although less prominently than in multigrains, the amplitude of LP peaks also increases and narrows with size. In multigrain, (i) the amplitude of the LP peaks grows and narrows with size. Remarkably, Pasquini *et al.*²¹ observed a similar build-up of longitudinal phonons of nanocrystalline α -Fe.²² (ii) Similarly to lh, a frequency tail appears at high frequencies. (Arrows also point to features arising from inner atoms.)

Finally, let us mention that Derlet and Swygenhoven²³ have recently shown that the features at higher frequencies in the DOS of nanocomposites originate from vibrations strongly localized in grain boundaries. The frequency tail that appears in $g(\nu)$ for lh and multigrain is an intrinsic feature of nanoscopic metals with grain boundaries. This remarkable finding reveals the strong connection between extended nanocrystalline materials and finite size nanoscopic grains.

C. Phonon localization

The participation ratio $N_{eff}(\nu)$ (see Appendix) indicates the effective number of atoms participating in a phonon with frequency ν . Thereby, $N_{eff}(\nu)$ measures the degree of phonon localization. In a sample with N atoms, $N_{eff} \simeq N/2$ for extended, wave-like phonon modes.²⁴ Note that when we identify a phonon mode as being localized [$N_{eff} \sim \mathcal{O}(1)$] we do not imply necessarily that the amplitude of the atomic vibrations decays away exponentially from a particular atomic site, as it is the case for Anderson-localized vibrational states.²⁵ In addition, while Anderson localization takes place in disordered systems, the term localization in the context of our results is broader as grains have a surface and, therefore, phonon localization—i.e., phonon modes with a small number of atoms involved in the vibration—takes place even in crystalline grains.

Figure 7 shows $N_{eff}(\nu)$ scaled by N , and the reduced vibrational density of states $g(\nu)/\nu^2$ for $N=459$ TO⁺, spherical and multigrain. The central results can be summarized as follows. (a) General features of N_{eff} are representative for all nanograins: (i) High-frequency phonons become more localized in both single-crystalline and multigrain specimens. In the latter, grain boundaries lead to a higher degree of localization. This is similar to what occurs in nanocrystalline materials;²³ a result that shows that nanograins capture some of the physics of their massive, nanocrystalline counterparts.²⁶ (ii) At low frequencies, the more localized the vibrations the higher the enhancement of DOS. In particular, spherical grains show a peak (arrow, Fig. 7) around 0.6 THz due to localized phonon modes at the surface protrusions. In turn, multigrain shows a similar enhancement due to phonons localized around vertex vacancies. In particular, two low-frequency modes at 0.1 THz and 0.3 THz that involve ~ 5 and 50 atoms, respectively, are responsible for the low-

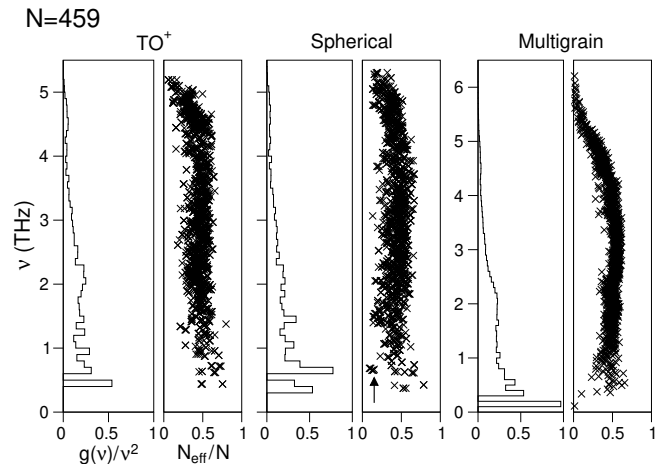


FIG. 7: Morphology effects on the reduced density of states $g(\nu)/\nu^2$ and the effective number of atoms $N_{eff}(\nu)$ in a phonon of frequency ν . For wave-like modes, $N_{eff}/N = 1/2$. Only multigrain shows a ν^2 distribution from 1 to slightly over 2 THz. In all grains, edges and vertices significantly enhance $g(\nu)/\nu^2$ below 1 THz. An arrow indicates modes heavily localized on the protrusions of the spherical grain, which coincide with the peak around 0.5 THz. In the multigrain, grain boundaries and irregular surfaces are responsible for the reduced fluctuations shown in N_{eff}/N .

frequency peak in $g(\nu)/\nu^2$. Faceted single-crystal and twined samples (not shown) show a lesser enhancement, arising only from the edges and vertices. (iii) N_{eff} significantly fluctuates around $N/2$ for single-crystal samples, twined lh and M-Dh; whereas in multigrain, irregular shape, surface disorder, and defects reduce these fluctuations.

(b) Two prominent features appear in $g(\nu)/\nu^2$: (i) The nearly quadratic behavior of $g(\nu)$ from 1 – 2.2 THz for multigrain. The frequency extent of this Debye-like [$g(\nu) \sim \nu^2$] region depends on the nature of disorder and defects—multiple grain boundaries, stacking faults, and vertex vacancies. Such Debye dependence has been observed in iron nanocomposites by Pasquini and coworkers.²¹ The Debye constant derived from the quadratic interval is nearly twice as big as the bulk value for Ag. Remarkably, such enhancement of the Debye constant has also been observed by Fultz and coworkers in nanocrystalline iron.²⁷ It should be noted that while we have found Debye-like behavior in a few nanograins of different sizes, the statistics we have is limited due to the intrinsic difficulty in generating competitive (Sec. II) multigrain samples using long molecular-dynamics simulations. (ii) The dramatic correlation between $N_{eff}(\nu)$ and $g(\nu)/\nu^2$, which shows that the degree of phonon localization in nanoscopic metal grains can be derived from a measurement of their vibrational density of states, after dividing by ν^2 .

IV. SUMMARY

To understand in detail the vibrational properties of nanoscopic metal grains we performed atomistic simulations of the phonon spectra—frequencies and displacement vectors—of silver grains with realistic morphologies. Our results show that morphology introduces a high degree of complexity into the phonon spectra, total and partial vibrational density of states, and phonon localization. The most prominent features are the following. (a) Low-energy, single-crystalline grains present nearly-pure torsional and radial phonon modes. The grains’ sharp edges and atomic lattice split off the acoustic gap quintet predicted by ET into a doublet and triplet, with a magnitude that depends on the relative number of atoms at the boundary of different facets. When compared to faceted grains of the same size, high-energy, spherical models that present regular protrusions on the surface have a smaller acoustic gap and a higher total DOS at frequencies $\nu < 2$ THz. (b) Twined icosahedra also have a breathing mode. Strain in these grains leads to a higher acoustic gap, and a high-frequency tail in the DOS that originates from core atoms. This tail extends beyond the highest frequency in single-crystalline grains. Remarkably, *neither* twined and strained Mark’s decahedra have a breathing mode nor do they exhibit a high-frequency tail on the DOS. (c) Nanograins with grain boundaries and surface disorder do not have degenerate frequencies and the acoustic gap is significantly reduced. These nanograins are the only ones that exhibit low-frequency ν^2 DOS in the interval 1-2THz. The extent of this region depends on the nature of disorder.

These predictions, while illustrated here for silver, should be valid for other nanoscopic metal grains. Our simulations show the complexity of the vibrational properties of metal nanograins, and point out similarities between the vibrational density of states of metal nanograins with grain boundaries and surface disorder and that of massive nanocrystalline samples. Finally, this work is a necessary step toward understanding the size-dependent electron-phonon coupling in nanoscopic metals.

Acknowledgments

Funds from U. S. DOE grant DE-F G02-99ER45795 and computational resources from the National Center

of Supercomputer Applications (NCSA) made this research possible. National Science Foundation grant NSF-DMR99-76650 supports the Materials Computation Center. We thank Professor Jian-Min Zuo (UIUC) for fruitful discussions. This research started at the Materials Computation Center (MCC). G.A.N. acknowledges its hospitality, and the opportunity to participate in the MCC Visitor Program.

APPENDIX A: METHODS

Nanograin’s structure and energetics. The literature contains extensive studies regarding the energetics of metal clusters. In this work, we consider known geometries and perform total energy relaxations in Ag nanograins. We also perform extensive simulated annealing to get complex, partially disordered morphologies.²⁸ To calculate the total energy \mathcal{E} we employ Daw and Baskes’ embed atom method²⁹ (EAM). We use Voter and Chen’s parametrization of Ag potential.

Vibrational properties. Once we generate stable nanograin morphologies we calculate phonon frequencies ν and displacement vectors $\{\vec{u}_\nu^i\}$ —where i labels an atom located at equilibrium position \vec{R}^i in the grain—by direct diagonalization of the dynamical matrix $D_{\alpha\beta}^{ij} = \partial^2 \mathcal{E} / \partial R_\alpha^i \partial R_\beta^j$. \vec{R}_α^i is a cartesian component ($\alpha, \beta = x, y, z$) of \vec{R}^i . Note that we consider free-standing nanograins, hence, the first six phonons correspond to rigid-body translations and rotations along and about the principal axis, respectively. These frequencies do not enter in our analysis.

The vibrational density of states (DOS) $g(\nu) = \sum_{j=1}^N g_j(\nu)$, where $g_j(\nu)\Delta\nu = (1/N) \sum_\nu n(\nu) \sqrt{M} |\vec{u}_\nu^j|$ is the partial (local) vibrational density of states at atomic site j ; \vec{u}_ν^j is the displacement vector of atom j ; $n(\nu)$ is the number of phonons between ν and $\nu + \Delta\nu$; and M is the mass of a Ag atom.

The equality $N_{eff}(\nu) = M_1^2/M_2$ defines the participation ratio.^{30,31,32} Here, $M_p = \sum_i^N [\varepsilon_i(\nu)]^p$ are momenta of the *mean* kinetic energy $\varepsilon_i(\nu)$ of atom i . By using the calculated displacement vectors of atom i in a phonon with frequency ν one readily calculates $\varepsilon_i(\nu)$.

* Current address: National Renewable Energy Laboratory, Golden, Colorado 80401.

¹ A. Arbouet, C. Voisin, D. Christofilos, P. Langot, N. Del Fatti, F. Vallée, J. Lermé, G. Celep, E. Cottancin, M. Gaudry, M. Pellarin, M. Broyer, M. Maillard and M. P. Pileni, and M. Treguer, Phys. Rev. Lett. **90**, 177401 (2003).

² J. Hodak, A. Henglein, and G. V. Hartland, J. Chem. Phys.

112, 5942 (2000).

³ B. A. Smith, J. Z. Zhang, U. Giebel, and G. Schmid, Chem. Phys. Lett. **270**, 139 (1997).

⁴ C. L. Cleveland, W. D. Luedtke, and Uzi Landman, Phys. Rev. B **60**, 5065 (1999); C. L. Cleveland, U. Landman, T. G. Schaaff, M. N. Shafigullin, P. W. Stephens, and R. L. Whetten, Phys. Rev. Lett. **79**, 1873 (1997); C. L. Cleve-

- land, U. Landman, M. N. Shafigullin, P. W. Stephens, and R. L. Whetten, *Z. Phys. D* **40**, 503 (1997).
- ⁵ F. Baletto, R. Ferrando, A. Fortunelli, E. Montalenti, and C. Mottet, *J. Chem. Phys.* **116**, 3856 (2002).
 - ⁶ F. Baletto, C. Mottet, and R. Ferrando, *Chem. Phys. Lett.* **354**, 82 (2002); *Phys. Rev. B* **63**, 155408 (2001).
 - ⁷ F. Baletto and R. Ferrando, *Rev. Mod. Phys.* **77**, 371 (2005).
 - ⁸ A. Kara and T. S. Rahman, *Phys. Rev. Lett.* **81**, 1453 (1998).
 - ⁹ D. Y. Sun, X. G. Gong, and X.-Q. Wang, *Phys. Rev. B* **63**, 193412 (2001).
 - ¹⁰ R. Meyer, L. J. Lewis, S. Prakash, and P. Entel, *Phys. Rev. B* **68**, 104303 (2003).
 - ¹¹ One may argue that such grains would be energetically unfavorable; however, these are more competitive than the simple models; see Sec. II.
 - ¹² L. D. Landau and E. M. Lifshitz, *Theory of Elasticity* (Pergamon Press, 1975).
 - ¹³ K. R. Patton and M. R. Geller, *Phys. Rev. B* **67**, 155418 (2003).
 - ¹⁴ A. Tamura, K. Higeta, and T. Ichinokawa, *J. Phys. C: Solid State Phys.* **15**, 4975 (1982).
 - ¹⁵ Variants of lh are those that include vertex and on-center vacancies. As first shown in Mottet, Tréglia, and Legrand, *Surf. Sci.* **383**, L719 (1997), our simulations also predict that the cohesive energy of on-center-vacant icosahedra improves slightly over lh; as the vacancy helps to relieve the accumulated strain. The cohesive energy does not improve by adding vertex vacancies in lh.
 - ¹⁶ C. Y. Yang, *J. Crystal Growth* **47**, 274 (1979), and references therein.
 - ¹⁷ L. D. Marks, *Rep. Prog. Phys.* **57**, 603 (1994), and references therein.
 - ¹⁸ Here, *sphericity* means how oblate the grain is. A comparison of the momenta of inertia along principal axes of a grain and a sphere measures the actual degree of sphericity. See K. Manninen, J. Akola, and M. Manninen, *Phys. Rev. B* **68**, 235412 (2003) where the authors correlate the momenta of inertia with the total energy of ultra-small ($N < 110$) Al nanograins.
 - ¹⁹ O. L. Anderson, *Physical Acoustics—Principles and Methods*, Vol. III—Part B, W. P. Mason Ed. (Academic Press, New York, 1965).
 - ²⁰ Other choices of bin size give similar results.
 - ²¹ L. Pasquini, A. Barla, A. I. Chumakov, O. Leupold, R. Rüffer, A. Deriu, and E. Bonetti, *Phys. Rev. B* **66**, 073410 (2002).
 - ²² Note that α -Fe nanocrystalline samples used in the experiments of Ref. 21 are not free-standing nanograins. They consist of *several* nanocrystals of nearly the same size that are prepared from a powder. The typical size of the nanocrystals depends on the synthesis and varies from nearly 6-13 nm.
 - ²³ P. M. Derlet and H. Van Swygenhoven, *Phys. Rev. Lett.* **92**, 035505 (2004); P. M. Derlet, R. Meyer, L. J. Lewis, U. Stuhr, and H. Van Swygenhoven, *Phys. Rev. Lett.* **87**, 205501 (2000).
 - ²⁴ For example, in a linear harmonic chain $N_{eff}/N = 1/2$ at all frequencies.
 - ²⁵ J. D. Maynard, *Rev. Mod. Phys.* **73**, 401 (2001).
 - ²⁶ The similarity between the DOS of nanoscopic grains and massive, nanocrystalline specimens depends on considering a range of grain's morphologies, in contrast to Meyer *et al.*¹⁰ who only compared spherical grains and a model nanocomposite.
 - ²⁷ B. Fultz, C. C. Ahn, E. E. Alp, W. Sturhahn, and T. S. Toellner, *Phys. Rev. Lett.* **79**, 937 (1997).
 - ²⁸ Our simulated annealing is based on molecular dynamics. We use Verlet's algorithm with time steps from 1-2 fs, and run multi-million-step simulations in the microcanonical ensemble. Typically, we cool down a molten droplet down to 300-500 K at rates from 20-50 K/ns. Then, we relax the atomic positions to minimize \mathcal{E} . Although we use high cooling rates, they are practical and fall within the range normally used in the literature.
 - ²⁹ M. S. Daw and M. I. Baskes, *Phys. Rev. B* **29**, 6443 (1984); *Phys. Rev. Lett.* **50**, 1285 (1983).
 - ³⁰ W. Jin, P. Vashishta, R. K. Kalia, and J. P. Rino, *Phys. Rev. B* **48**, 9359 (1993).
 - ³¹ S. R. Nagel, G. S. Grest, and A. Rahman, *Phys. Rev. Lett.* **53**, 368 (1984).
 - ³² P. T. Dean, *Rev. Mod. Phys.* **44**, 127 (1972).